ELSEVIER

Journal of Hazardous Materials B136 (2006) 219–232

Journal of Hazardous Materials

www.elsevier.com/locate/jhazmat

# Model of large pool fires

J.A. Fay *

*Department of Mechanical Engineering, Massachusetts Institute of Technology, Cambridge, MA 02139, USA*

Received 22 July 2003; received in revised form 25 September 2005; accepted 8 November 2005
Available online 25 January 2006

**Abstract**

A two zone entrainment model of pool fires is proposed to depict the fluid flow and flame properties of the fire. Consisting of combustion and plume zones, it provides a consistent scheme for developing non-dimensional scaling parameters for correlating and extrapolating pool fire visible flame length, flame tilt, surface emissive power, and fuel evaporation rate. The model is extended to include grey gas thermal radiation from soot particles in the flame zone, accounting for emission and absorption in both optically thin and thick regions. A model of convective heat transfer from the combustion zone to the liquid fuel pool, and from a water substrate to cryogenic fuel pools spreading on water, provides evaporation rates for both adiabatic and non-adiabatic fires. The model is tested against field measurements of large scale pool fires, principally of LNG, and is generally in agreement with experimental values of all variables.


*Keywords:* Pool fire; Entrainment model; Grey gas model; Thermal radiation; LNG

## 1. Introduction

The understanding of the properties of pool fires has been driven recently by concern over safety issues. The size, duration and thermal radiation emissions of pool fires are the principal features that affect safety assessments of accidental fires. In particular, pool fires formed by unconstrained spills of large volumes of liquid fuels onto water can reach sizes of the order of several hundred meters in diameter [1], well beyond the experimental scale available for study in the laboratory or largest field tests. Extrapolating test data to such large pool fires requires careful analysis of the scaling laws for pool fire characteristics.

Experimental observations of laboratory and field tests have centered on the rate of combustion of fuel mass per unit pool area, the size and shape of the visible flame zone, the effects of a cross wind on the flame size and shape, and the thermal radiation from the pool fire. These have been found to depend upon the fuel type, the pool area and shape, ambient meteorological conditions, and the possible presence of substrate heating of the fuel pool. Various empirical relationships were established between these observable and the independent parameters of the experiments (see [2–5]).

Thomas [6] noted that the structure of a pool fire could be related to that of a thermal plume if one identified the plume buoyancy flux, a constant of the motion, with that generated by the combustion of the fuel in a pool fire. Using dimensional arguments, the observations of vertical speeds in buoyancy-dominated fires, and the plume model of Morton et al. [7], Thomas concluded that the ratio of visible flame length to pool diameter should be proportional to the two-thirds power of the fuel Froude number $F_f$ (see equation [3] below). Thomas used these variables to correlate flame height measurements for wood crib fires, finding a slightly smaller exponent than 2/3 for the dependence upon Froude number.

On the other hand, there is an extensive literature on the properties of jet flames (see [2,5]), where it is convincingly shown that the visible flame length is proportional to the 2/5 power of $F_f$. Furthermore, the range of $F_f$ available in these experiments spans five orders of magnitude, so the correlation is quite pronounced. Even more significant, the correlation is exactly what is expected if the jet flame is modeled as a thermal plume as described by Morton et al. [7]. Measurements of jet flame centerline temperature and velocity in the region of the flame tip and beyond also conform to the thermal plume model [8].

In jet flames, the fuel vapor source velocity, and thereby $F_f$, are variable over a wide range. In contrast, pool fire vapor velocities are determined by feed back of heat from the flame to evaporate the fuel, lying within a small range of 0.02–0.1 m/s,

* Tel.: +1 617 253 2236; fax: +1 617 258 8559.
*E-mail address:* jfay@mit.edu.

0304-3894/$ – see front matter © 2005 Elsevier B.V. All rights reserved.
doi:10.1016/j.jhazmat.2005.11.095

depending upon fuel volatility [3,4], and the range of $F_f$ is less than an order of magnitude. As a consequence, the ratio of flame length to diameter is much smaller for pool fires than jet flames [2] and the combustion is completed at a height less than the pool diameter.

The measurement of the visible luminous flame length is dependent on optical band radiation from thermally heated soot particles, which is not explicitly relatable to the flow variables of the thermal plume model. Steward [10] noted that, for jet flames, the visible plume height corresponded to the location in the thermal plume model where the average equivalence ratio of the plume gases was about 0.2; that is, the mass ratio of stoichiometric combustion products to plume gas was 20% and where the mean temperature excess in the plume would be 20% of that of an adiabatic premixed flame.[1] Alternatively, Heskestad [2] located the flame tip at a point where the centerline flame temperature excess above ambient is about 500 K. These conditions are equivalent; they identify the flame tip as a point where the flame products have been diluted well below the stoichiometric value and is well beyond the zone where the fuel is reacting with entrained air. In this region, the plume centerline temperature varies as the −5/3 power of the distance along the plume [2] and the grey gas emissive power would decline as the fourth power of the absolute temperature. The optical band luminosity declines even more precipitously since it lies in the exponentially decreasing portion of the grey gas spectrum.

In this paper an entrainment model is used to describe the fluid motion within a pool fire resulting from the turbulent diffusion flame established by the combustion of the fuel evaporated from the pool surface. The model identifies two zones, the combustion zone at the base of the fire and a visible flame zone above it.[2] The model allows the determination of the visible flame length and tilt angle in a cross wind, to within three dimensionless empirical constants determined by comparison with field experiments. By making simplifying but plausible assumptions about flame soot concentrations, a thermal radiation model consonant with the pool fire model provides a determination of thermal radiation from the pool fire that is dependent upon two empirical constants determined from field tests. This model shows the reduction in fire thermal flux from soot absorption to be expected from very large scale pool fires. A modeling of the heat transfer from the hot combustion gas to the pool liquid fuel correlates the observed evaporation rates in adiabatic confined pool fires. Additionally, a model of incremental evaporation rate for pool fires on water explains the observed enhanced evaporation rates for such fires.

## 2. Entrainment model

A pool fire is a diffusion flame driven entirely by gravitational buoyancy. Nevertheless, it possesses many of the characteristics of non-buoyant jet diffusion flames [11,12]. Fig. 1 is a sketch of the fluid flow field of a circular pool fire burning in a stationary atmosphere, showing a vertical plane of the axisymmetric flow. The fire is shown as having a lateral surface in the form of a circular cylinder of diameter $D$ and height $L_v$, somewhat greater than $D$, as is commonly observed. Fuel is supplied to the core of the fire by evaporation from the liquid pool surface, the latter process being driven by heat transferred from the fire to the liquid fuel, as well as heat transfer from the pool substrate, when present. Air is entrained through the exterior surface of the fire region, due to the vertical motion of the hot gases in the fire. These two flows of fuel and air meet at the flame surface, where they combine in stoichiometric proportions to produce combustion products. The products subsequently mix with entrained air as they rise further, as in a thermal plume.

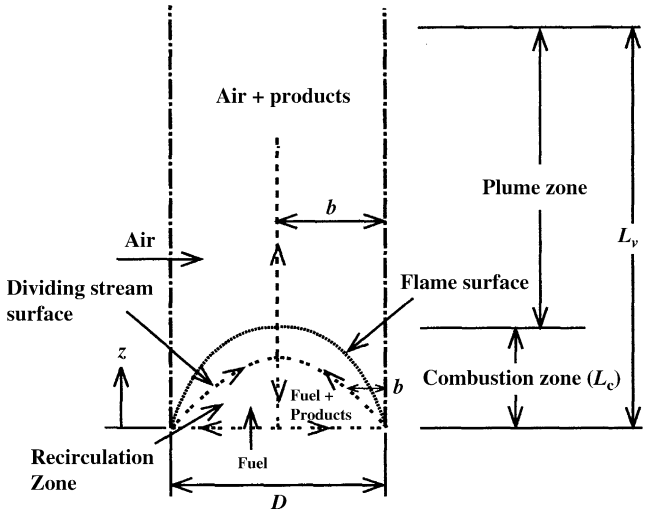


Fig. 1. A schematic sketch of the cross-section of a pool fire, showing the fluid flow zones and dimensions.

It is convenient to divide the pool fire into two parts; the lower combustion zone and the upper plume zone (see Fig. 1). In the combustion zone, fuel and air are mixed and react to form products in stoichiometric proportions. The burned gas axial velocity increases rapidly in the vertical direction, as do the vertical fluxes of mass, momentum and thermal energy in the fire. In the plume zone, which begins at the upper edge of the combustion zone where all the fuel has been consumed, there is no further increase in thermal energy flux, yet the mass and momentum fluxes continue to increase. Continued air entrainment is accompanied by declines in temperature, concentration of combustion products, and axial speed.

Unlike a jet diffusion flame, where the fuel flow initially provides a considerable upward momentum flux, the feeble fuel vapor flow in a pool fire is entrained in a recirculation zone, which initially carries fuel radially outward to the flame surface at the outer edge of the pool, then upward and inward toward the axis, supplying fuel to the flame surface above it. The upper surface of this recirculation zone is a dividing stream surface, separating the outer flow moving inward and upward toward the top of the fire, from the inner flow, which circulates downward

[1] Fay and Lewis [9] note an equal equivalence ratio for the visible limit of burning fireballs in laboratory experiments.

[2] Steward [10] employed a model of jet fires that included a region near the jet exit within which the fuel was completely burned to stoichiometric proportions. It differs in significant ways from the model of this paper, which applies only to pool fires.

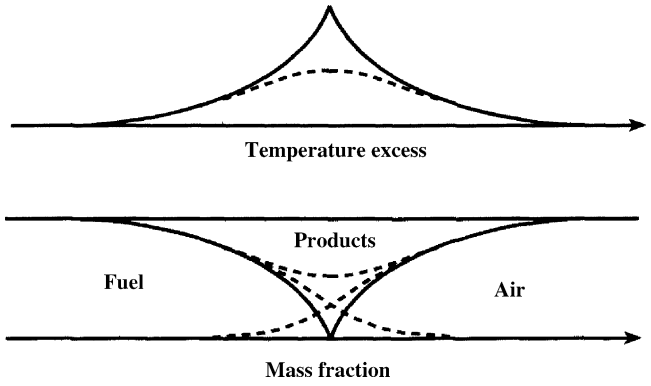


Fig. 2. A sketch of the distribution of flow variables within a diffusion flame as a function of the distance normal to the flame surface in the direction of the flow (left to right); temperature excess above air background (above) and mass fraction of reactants and products (below). Solid line for laminar and dashed line for turbulent flames.

near the axis and then outward along the pool surface, as in Fig. 1.[3]

In the combustion zone, both fuel and air diffuse toward the flame surface, and are convected upward by the fluid flow within the flame zone. The combustion at the flame surface releases heat which, like products, diffuses away from the flame surface, raising the temperature and reducing the density of the flame zone gas. This low density gas is accelerated upward by the imbalance in gravity and pressure forces, providing upward momentum of the flame zone gas. At the top of the flame surface, where all the fuel vapor leaving the pool has been burned, only air and combustion products remain. Further vertical travel of this flow develops as in a buoyant plume [7,10,5].

The distributions of temperature and mass fraction of chemical species in a laminar diffusion flame are sketched in Fig. 2 (solid lines), as a function of the distance normal to the flame surface in the direction of fluid flow. Upstream of the flame surface (left side of the figure), convection and diffusion deliver fuel to the reaction zone, a thin layer between the upstream and downstream regions of fuel and air supply, respectively. On the downstream side, air diffuses upstream but is convected downstream, the former overcoming the latter to supply enough air to react with the fuel. Combustion products, produced in the reaction zone, diffuse both upstream and downstream, but the convective flow sweeps them downstream. Since the fuel combustion is a source of heat as well as products, the temperature distribution in the flame is similar to that of the products, reaching a maximum in the reaction zone equal to the adiabatic flame temperature $T_{ad}$. For the combustion reaction to occur, the fuel and air must be mixed at the molecular level, which occurs in the reaction zone.

In a turbulent diffusion flame, the spatial extent and distribution of flow variables is different in some respects from those in a laminar flame, as illustrated in the dashed lines of Fig. 2. First of all, there are large fluctuations in these variables about the their time-averaged values depicted in Fig. 2. The reaction zone occupies a larger fraction of the flame region where, on average, fuel, air, and products exist simultaneously due to the vigorous eddy mixing processes. The average peak temperature is less than the adiabatic flame temperature because a temperature probe mostly samples larger and cooler fuel- or air-rich eddies than the smallest eddies within which molecular mixing is complete, combustion reactions occur rapidly, and the adiabatic flame temperature is reached. Secondly, the thickness of the diffusion flame is greater than in the laminar case because the turbulent diffusivities are orders of magnitude greater than molecular diffusivities.

In both laminar and turbulent diffusion flames, it can be shown [11] that linear relationships exist among the scalar variables temperature $T$, axial flow speed $w$, and species mass fraction $\chi_i$ if the thermal, viscous and species diffusivities are equal to each other. While these diffusivities are not exactly equal, and the linear relationships only approximate, they provide a simple understanding of the flame structure that is helpful. For example, the product mass fraction $\chi_p$ is related to the temperature $T$ by:

$$\chi_p = \frac{T - T_a}{T_{ad} - T_a} \tag{1}$$

where $T_a$ is the ambient temperature. This relationship is consistent with the sketch of Fig. 2.

In hydrocarbon fuel–air flames, whether laminar or turbulent, the ratio of mass flow rate of air to that of fuel needed to completely burn the fuel is in the range of 15–17. The diffusive flow of air into the flame surface limits the rate of consumption of fuel in the combustion zone. About 80% of the air mass or product mass is nitrogen, which does not enter into the combustion reactions, but is a diluent that carries most of the mass, momentum, and thermal energy fluxes in the flame. One can think of the diffusion flame as a nitrogen dominated flow in which the minor species of fuel and oxygen react to form carbon dioxide and water vapor, releasing thermal energy to the nitrogen. Of these species, the fuel mass flux is generally the smallest.

In the following subsections, we develop integral forms for the conservation of mass, energy, and momentum for the flow in the pool fire. In so doing, we make certain assumptions regarding the inflow of air that are similar to those used in buoyant plumes, jets, and wakes. In this case, the principal assumption is that the mass flow rates of air into the flame are proportional to the upward mass flow rate within the flame.

There is an immediate consequence of this assumption and the scaling law for fluid velocities that leads to the determination of the combustion zone height $L_c$. The magnitude of the mass inflow rate of air into the flame is proportional to $\rho_a\sqrt{gL_c}L_cD$, where $\rho_a$ is atmospheric density. But the mass inflow rate of fuel is proportional to $\dot{m}D^2$, where $\dot{m}$ is the mass evaporation rate of fuel per unit area of the pool surface. Since these mass flow rates are proportional to each other, we find

$$\frac{L_c}{D} \propto \left(\frac{\dot{m}}{\rho_a\sqrt{gD}}\right)^{2/3} \tag{2}$$

[3] This recirculation zone is similar to that in the wake behind a bluff body in a uniform flow where the shear in the external separated flow induces a low speed recirculation in the immediate wake. In the pool fire, the flame surface provides the shear needed to generate the recirculation.

The dimensionless fraction on the right, which we shall call the fuel Froude number $F_f$,

$$F_f \equiv \frac{\dot{m}}{\rho_a \sqrt{gD}} \tag{3}$$

was introduced by Thomas [6] as the dimensionless parameter determining the ratio $L_v/D$ of visible flame height $L_v$ to diameter $D$. As discussed above, the visible flame height of jet diffusion flames scales as $F_f^{2/5}$ because the visible limit lies within the plume zone, where the relationship of (2) does not apply. It will be seen below that (2) expresses the scaling law for the combustion zone.

### 2.1. Conservation of mass, energy and vertical momentum

Consider the mass flow across a horizontal plane at a height $z$ above the pool fire base (see Fig. 1). Denoting the $z$-component of velocity by $w$, the gas density by $\rho$, and the radial distance from the flame axis by $r$, the mass flux $M$ becomes:

$$M = \int_0^\infty \rho w (2\pi r \, dr) \tag{4}$$

While the integration extends from 0 to infinity on $r$, only within a limited area $A$ of this horizontal plane is there any appreciable contribution to this integral. We may thus write the integral as

$$M = \int_0^A \rho w \, dA \tag{5}$$

To better define the size of $A$, introduce a radial length $b$, different for the combustion and plume zones, to define $A_c$ and $A_p$ as

$$A_c \equiv \pi D b \quad \text{(combustion)} \tag{6}$$

$$A_p \equiv \pi b^2 \quad \text{(plume)} \tag{7}$$

The axial fluxes ($M_i$, $P$, $E$) of species, momentum, and enthalpy become

$$M_i = \int_0^A (\rho w) \chi_i \, dA \tag{8}$$

$$P = \int_0^A (\rho w) w \, dA \tag{9}$$

$$E = \int_0^A (\rho w) c_p (T - T_a) \, dA = c_p T \int_0^A w(\rho_a - \rho) \, dA \tag{10}$$

where $c_p$ is the (constant) specific heat of the flame gas and where diffusional fluxes of species mass and enthalpy, and normal shear stress, are neglected. The form of (8)–(10) emphasizes the convective transport of the scalar variables $\chi_i$, $w$, and $c_p(T - T_a)$. The alternate form for $E$ is proportional to the buoyancy flux.[4]

[4] The bouyancy flux is conventionally defined as $\int_0^A wg(1 - (\rho/\rho_a)) \, dA$.

The mass flux $M$ increases with height $z$ by entrainment of air,

$$\frac{dM}{dz} = \alpha_c \left( \frac{\rho_a P}{M} \right) D \quad \text{(combustion)} \tag{11}$$

$$= \alpha_p \sqrt{\rho_a P} \quad \text{(plume)} \tag{12}$$

where the entrainment rate is expressed in terms of the fluxes $M$ and $P$ and a dimensionless form factor $\alpha$, different for each zone.[5]

The axial momentum increases because of the buoyant force

$$\frac{dP}{dz} = \int_0^A g(\rho_a - \rho) \, dA = \eta_c \left( \frac{g}{c_p T_a} \right) \left( \frac{EM}{P} \right) \quad \text{(combustion)} \tag{13}$$

$$\frac{dP}{dz} = \int_0^A g(\rho_a - \rho) \, dA = \eta_p \left( \frac{g}{c_p T_a} \right) \left( \frac{EM}{P} \right) \quad \text{(plume)} \tag{14}$$

where the buoyant force is expressed in terms of the fluxes $E$, $M$, and $P$ and a dimensionless form factor $\eta$.

Finally, the enthalpy flux increases where fuel reacts with the entrained air in the combustion zone

$$\frac{dE}{dz} = \phi_c \left( \frac{h_c}{f} \right) \frac{dM}{dz} \quad \text{(combustion)} \tag{15}$$

where $h_c$ is the fuel heating value per unit mass of fuel, $f$ is the mass ratio of product to fuel in a stoichiometric mixture, and $\phi_c$ is the combustion zone equivalence ratio, the ratio of the fuel/air mass consumed compared with its stoichiometric value.[6]

On the other hand, in the plume zone $E$ remains constant at a value determined by the rate of fuel vaporization

$$E_p = \dot{m} h_c \left( \frac{\pi D^2}{4} \right) = \left( \frac{\pi}{4} \right) h_c \rho_a g^{1/2} D^{5/2} F_f \quad \text{(plume)} \tag{16}$$

Eqs. (11)–(16), together with suitable initial conditions, provide a solution for the fluxes $M$, $P$ and $E$ as functions of axial distance $z$, for both the combustion and plume zones.

#### 2.1.1. The combustion zone

The combustion zone extends from the pool surface ($z = 0$) to the height at which all the fuel has been burned ($z = L_c$). At the pool surface, $E = 0$ while $P$ and $M$ are very small compared to their values at the top of the combustion zone, and hence can be considered zero for practical purposes. As a consequence, throughout this zone $E$ and $P$ are related to $M$ by integrals of (13)–(15)

$$E = \phi_c \left( \frac{h_c}{f} \right) M \tag{17}$$

[5] Ricou and Spaulding [13] pointed out that the form for the plume follows from a dimensional analysis for an axially symmetric jet. The form for the combustion zone is that for a plane jet or plume, for which they find $\alpha_p = 0.28$.

[6] The ratio $h_c/f$, the enthalpy change in the combustion reaction per unit mass of product, varies little among common fuels.

$$P = \left[\frac{3}{4}\left(\frac{\eta_c\phi_c}{\alpha_c}\right)\left(\frac{h_c}{fc_pT_a}\right)\left(\frac{gM^4}{\rho_a D}\right)^{1/3}\right] \tag{18}$$

and $M$ is determined from the integral of (11),

$$M = \alpha_c\rho_a D\left[\frac{2}{9}\left(\frac{\eta_c\phi_c}{\alpha_c}\right)\left(\frac{h_c}{fc_pT_a}\right)\right]^{1/2} g^{1/2}z^{3/2} \tag{19}$$

Mass flow averaged values of velocity $\bar{w}$ and temperature $\bar{T}$ in the combustion zone are found to be

$$\bar{w} \equiv \frac{P}{M} = \left[\frac{1}{2}(\eta_c\phi_c)\left(\frac{h_c}{fc_pT_a}\right)\right]^{1/2}\sqrt{gz} \tag{20}$$

$$c_p(\bar{T} - T_a) \equiv \frac{E}{M} = \phi_c\left(\frac{h_c}{f}\right) \tag{21}$$

Eqs. (20) and (21) show how $\bar{w}$ and $\bar{T}$ scale in the combustion zone; $\bar{w}$ is the proportional to $\sqrt{gz}$ while $\bar{T}$ is the independent of $z$. In contrast, it will be seen below that both decrease with increasing $z$ in the plume zone.

The flow area $A_c$ is determined to be

$$A_c \equiv \frac{M}{\rho_a\bar{w}} = \frac{2}{3}\alpha_c^{1/2}Dz \tag{22}$$

so that the area and dimension $b$ of Eq. (6) increase linearly with $z$.

Finally, the height of the combustion zone, $L_c$, may be found by setting $z = L_c$ when $E = E_p$, giving

$$\frac{L_c}{D} = \left(\frac{9\pi^2}{32}\right)^{1/3}\left(\frac{1}{\phi_c^3\eta_c\alpha_c}\right)^{1/3}\left(\frac{f^3c_pT_a}{h_c}\right)^{1/3}F_f^{2/3} \tag{23}$$

This is the precise relationship estimated in (2).

### 2.1.2. Plume zone

The buoyant plume zone extends upward from the end of the combustion zone ($z = L_c$). Within the plume zone the sensible enthalpy flux $E$ is constant at the value $E_p$ of Eq. (16), while the mass and momentum fluxes $M$ and $P$ increase with height in accordance with the relations (12) and (14). But in this region the average temperature $\bar{T}$ and velocity $\bar{w}$ decline with increasing $z$. At a point along this path, where visible radiation becomes negligible because the temperature has declined sufficiently by dilution with entrained air, the elevation $z$ is equal to the (visible) flame height $L_v$.

In principle, to find the plume zone variables we could integrate (12) and (14), starting at $z = L_c$ and using the initial values for $P$ and $M$ found from the combustion zone solutibn of Section 2.1.1. But the values of the dimensionless coefficients are unknown, and an analytic solution is not possible. Instead, we follow the approach of [2] and find a thermal plume solution, assuming $M$ and $P$ are zero at a virtual source located a distance $z_0$ below the pool surface. This solution has the virtue of becoming accurate at $z \gg L_c$, but at $z = L_c$ will give discontinuous values of $P$ and $M$, but not $E$, by amounts that depend upon $z_0$, and discontinuous values of all gradients.

Table 1
Scaling relations for combustion and plume zone variables

| | $\frac{\partial \ln(\text{Variable})}{\partial \ln z}$ | |
|---|---|---|
| Variable | Combustion | Plume |
| $M$ | 3/2 | 5/3 |
| $P$ | 2 | 4/3 |
| $E$ | 3/2 | 0 |
| $A$ | 1 | 2 |
| $b$ | 1 | 1 |
| $\bar{w}$ | 1/2 | −1/3 |
| $\bar{T} - T_a$ | 0 | −5/3 |

Integrating (12) and (14), we find

$$P = \left(\frac{5\eta_pE_p}{4\alpha_pc_pT_a\sqrt{\rho_a}}\right)^{2/5}M^{4/5} \tag{24}$$

$$M = \left(\frac{3^5}{4(5^4)}\right)^{1/3}\left(\frac{\eta_p\rho_a^2E_p\alpha_p^4}{c^pT_a}\right)^{1/3}(z + z_0)^{5/3} \tag{25}$$

and then determine $\bar{w}$, $\bar{T}$, and $A_p$ as

$$\frac{\bar{w}}{\sqrt{gD}} \equiv \frac{P/M}{\sqrt{gD}} = \left(\frac{25\pi}{48}\right)^{1/3}\left(\frac{\eta_ph_c}{\alpha_p^2c_pT_a}\right)^{1/3} \times F_f^{1/3}\left(\frac{z + z_0}{D}\right)^{-1/3} \tag{26}$$

$$\frac{\bar{T}}{T_a} - 1 \equiv \frac{E/M}{c_pT_a} = \left(\frac{\pi^2(5^4)}{4(3^5)}\right)^{1/3}\left(\frac{h_c}{\sqrt{\eta_p}\alpha_pc_pT_a}\right)^{2/3} \times F_f^{2/3}\left(\frac{z + z_0}{D}\right)^{-5/3} \tag{27}$$

$$A_p \equiv \frac{M}{\rho_a\bar{w}} = \alpha_p\left(\frac{3}{5}\right)(z + z_0)^2 \tag{28}$$

The pool fire variables, $M$, $P$, $E$, $A$, $b$, $\bar{w}$, and $\bar{T} - T_a$ appearing in Eqs. (4)–(28) above, are proportional to a power of $z$. In Table 1, we show the corresponding power in both the combustion and plume zones. All of these variables increase with $z$ in both zones, with the exception of $\bar{w}$ and $\bar{T} - T_a$ in the plume zone, which decrease. Mostly, the growth rates are higher in the combustion than in the plume zone, a consequence of the accelerating energy addition in the combustion zone.[7]

### 2.1.3. Visible flame length

As mentioned in Section 1, the observed visible flame length $L_v$ is sensitive to the decline in average temperature $\bar{T}$ with height $z$ in the plume, as in (27). For jet diffusion flames, Heskestad [2] suggests that $L_v$ is identified with a fixed value of the plume

[7] Except for the numerical and dimensionless factors, Eqs. (26)–(28) are equivalent to those of Steward [10] and Heskestad [5] for jet fire plumes.

centerline temperature, while Steward [10] shows a useful correlation based upon the value of the equivalence ratio $\phi_v$ in the plume at the visible flame tip. Accepting Steward's criterion, we suggest that the visible flame length is identified with the occurrence of an equivalence ratio $\phi_v$ at $z = L_v$ in the plume, where $\phi_v$ is related to the plume energy and mass fluxes by

$$\phi_v = \frac{fE_p}{h_c M|_{z=L_v}} \tag{29}$$

as in (17). By combining Eqs. (27) and (25) with the condition of (29), we find an expression for the visible flame length $L_v$,

$$\frac{L_v}{D} = -\frac{z_0}{D} + \left(\frac{\pi^2(5^4)^{1/5}}{4(3^5)}\right)^{1/5}\left(\frac{1}{\phi_v^3\eta_p\alpha_p^2}\right)^{1/5} \times \left(\frac{f^3 c_p T_a}{h_c}\right)^{1/5} F_f^{2/5} \tag{30}$$

### 2.1.4. Effect of fuel combustion properties

Both the combustion and plume zone heights, $L_c$ and $L_v$, are proportional to fractional powers of the dimensionless product $(f^3 C_p T_a/h_c)F_f^2$. Heskestad [2] notes that the dimensionless parameter $N$ (called the combustion number by Steward [10]), defined as

$$N \equiv \frac{\pi}{4}\left(\frac{f^3 c_p T_a}{h_c}\right) F_f^2 \tag{31}$$

correlates the visible length of turbulent jet flames for a large variety of fuels. The first factor on the right of (31) expresses the effect of the fuel heating value while the second expresses the effects of buoyancy. For alkane vapors, the factor $(f^3 C_p T_a/h_c)$ varies by 33% for carbon numbers 1–16, but is substantially higher for hydrogen and lower for methanol. The visible flame height, which is proportional to $N^{1/5}$, varies by about a factor of two between hydrogen and methanol, but only by 6% for alkane fuels, for a given value of $F_f$.[8]

### 2.1.5. Wind tilt

Before comparing this model with experimental observations, it is necessary to include the effects of a cross wind, which is observed to cause the flame to tilt through an angle $\theta$ from the vertical. But it is also observed that, for the most part, the slant length $L_v$ of the visible flame is only slightly affected by the cross flow (see Thomas [6]), so that

$$H_v \simeq L_v \cos\theta \tag{32}$$

Thus, the tilted flame height $H_v$ is observed to be reduced below the zero wind value even while the slant height $L_v$ remains unchanged.

To modify the pool fire model for the effects of a cross wind of velocity $V$, it is necessary to account for an increased entrainment

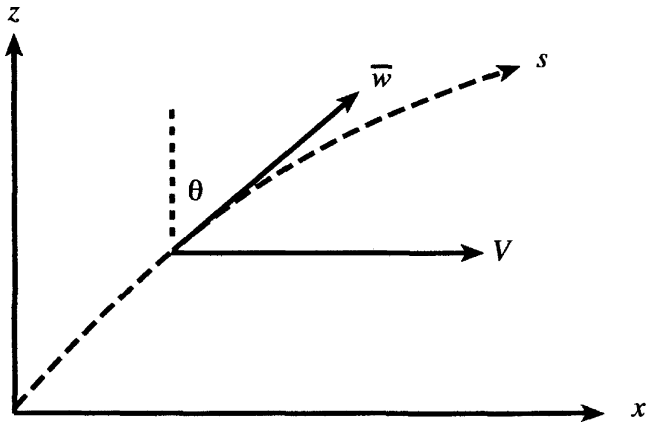


Fig. 3. A coordinate system for analyzing the wind tilt of fire plumes, $x$ is the downwind distance and $s$ is the distance along the streamline of the plume axis.

rate caused by the cross wind. In models of thermal plumes in a cross wind, which successfully explain their observed behavior, entrainment rates include components from both vertical and horizontal motion of the plume gas with respect to the atmosphere (see [14–16]). Using the coordinate system of Fig. 3 for the plume portion of the pool fire, we write the mass and momentum conservation along the plume centerline distance $s$, whose tangent makes an angle $\theta$ with the vertical, as

$$\frac{dM}{ds} = \alpha_p\sqrt{\rho_a P} + \left(\frac{M}{\sqrt{\rho_a P}}\right)(\beta_p\cos\theta - \alpha_p\sin\theta)V \tag{33}$$

$$\frac{dP}{ds} = \left(\frac{\eta_p g E_p}{c_p T_a}\right)\frac{M}{P}\cos\theta + (V\sin\theta)\left(\frac{dM}{ds}\right) \tag{34}$$

where $\beta_p$ is the entrainment coefficient for cross flow. For zero wind speed, where $\theta = 0$, (33)–(34) reduce to (12) and (14).

The momentum conservation normal to the plume centerline is

$$P\left(\frac{d\theta}{ds}\right) = -\left(\frac{\eta_p g E_p}{c_p T_a}\right)\frac{M}{P}\sin\theta + (V\cos\theta)\left(\frac{dM}{ds}\right) \tag{35}$$

By combining the streamwise and normal momentum equations, we find the integral relation

$$\sin\theta = \frac{VM}{P} = \frac{V}{\bar{w}} \tag{36}$$

which may be used to eliminate $\theta$ from (33) and (34), making it possible to determine $M$ and $P$ numerically as functions of $s$ and the parameter $V$.

For the purpose of further analysis, we consider only two limiting cases: $V$ is small compared with $\bar{w}$, the streamwise velocity at the flame tip, and $V$ is nearly equal to $\bar{w}$. We take the flame tilt angle to be the value of $\theta$ at the flame tip

$$\sin\theta \equiv \frac{V}{\bar{w}} = \frac{F_w\sqrt{gD}}{\bar{w}} \tag{37}$$

where $F_w \equiv (V/\sqrt{gD})$ is the wind Froude number. For the low wind case, the plume is nearly vertical and the maximum value of $\bar{w}$ is about $\sqrt{gD}$, so that $\sin\theta \sim F_w$. For the high wind case, $\bar{w} \sim V$ and $\sin\theta \sim 1$. In intermediate cases, there is a complex relation determined by the solution to (33) and (34). For the

[8] Heskestad [2] also introduces a dimensionless energy flux $Q^* \equiv (h_c/fc_pT_a)^{3/2}N^{1/2} = (\pi h_c/4c_pT_a)F_f$.

purpose of comparison with field tests, we propose that this relationship can be correlated in the form

$$\sin\theta = \frac{F_w}{F_w + c} \tag{38}$$

which has the limiting values discussed above, and where the constant $c$ is to be determined from the experimental observations.[9]

### 2.2. Unsteady flow effects

Large pool fires, like jet flames, have noticeable time-dependent variations in easily observed properties like plume dimensions, visible luminosity, and vertical speed. Like other free shear flows such as jets and wakes, large scale eddies seem to dominate this unsteadiness, with detectable frequencies and sizes. The dimensionless measure of such cyclic unsteadiness is the Strouhal number *Str*, defined as the product of the length scale times the frequency $\omega$ divided by the velocity scale. For a pool fire, if we choose the length scale as $D$ and the velocity scale as $\sqrt{gD}$, then the Strouhal number would be

$$Str = \omega\sqrt{D/g} \tag{39}$$

Measurements of $\omega$ in jet flames show that it is proportional to $D^{-1}/^2$ [5], leading to a value of 0.48 for *Str*. This is typical of the Strouhal number for large eddy structures in turbulent wakes and jets.

Fay and Lewis [9] suggest that a pool fire may be considered to be the equivalent of a series of fireballs. Their analysis of the combustion of a vapor cloud of volume $V$ leads to a visible flame height $L_v$ proportional to $V^{1/3}$, a burnout time proportional to $g^{-1/2}V^{1/6}$, and an average volumetric flow rate proportional to $g^{1/2}V^{5/6}$. Setting the latter proportional to the pool fire volumetric flow rate $\dot{m}D^2/\rho_a = F_f\, g^{1/2} D^{5/2}$ yields the proportionality

$$\frac{L_v}{D} \propto F_f^{2/5} \tag{40}$$

which is the equivalent of (30) for the visible flame length of a steady pool fire.

### 2.3. Comparison with pool fire tests

#### 2.3.1. Combustion zone

Compared with visible flame height measurements, those of the combustion zone height $L_c$ are very scarce since the latter require measuring the gas temperature within the combustion zone. Definitive temperature profiles in this region of adiabatic[10] heptane pool fires were made by Koseki and Yumoto [17]. Isotherms measured for a 6 m diameter pool fire showed a combustion zone flame surface, approximately conical in shape, extending from the outer rim of the pool to the fire axis at a point

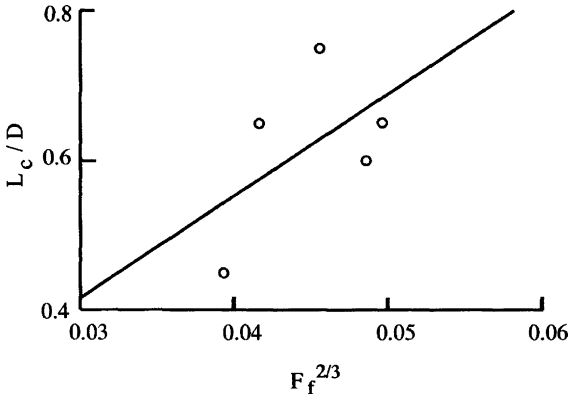


Fig. 4. A plot of the measured combustion zone height $L_c$ for heptane pool fires, compared with the correlation of (41).

where the centerline temperature reached a maximum. The elevation $z$ of the centerline temperature maximum for all tests was taken as the combustion zone height $L_c$.

These five tests covered a range of pool diameters from 0.3 to 6 m, fuel Froude number $F_f$ from (8 to 11) $\times 10^{-3}$, and $L_c/D$ from 0.45 to 0.75. These measurements, shown in Fig. 4, are correlated by (23) as

$$\frac{L_c}{D} = (13.8 \pm 2.15)F_f^{2/3} \tag{41}$$

in which the standard deviation of $L_c/D$ is 15.6% of the mean value. Koseki and Yumoto [17] also measure the mass flux in the pool fire, reported as a fraction of the stoichiometric value, which is the same as the equivalence ratio $\phi$. At $z = L_c$, $\phi$ has a measured value of $\phi_c \sim 1.7$. Using this value of $\phi_c$ and the thermal properties of heptane, by comparing (23) and (41), we calculate that $\sqrt{\alpha_c \eta_c} \sim 0.1$. Since $\alpha_c$ should be about 0.3 [13], we conclude that $\eta_c$ has about the same value.

#### 2.3.2. Plume zone

The visible flame length is determined from photographs that are sensitive to the visible spectrum, 0.4–0.8 $\mu$m. As there is no significant molecular radiation in this band, the visual light intensity is due to incandescent soot particles presumably in thermal equilibrium with the hot combustion and plume gas. The black body emissive power $\varepsilon_{vis}$ in the visible band from a surface at temperature $T$ is proportionately related to $T$ by

$$\varepsilon_{vis} \propto \exp\left(-\frac{(2060\text{K})}{T}\right) \tag{42}$$

provided $T \ll 2060$ K. Heskestad [2] notes that the plume centerline temperature at the flame tip of jet flames is 500–600 K, at which point $T - T_a$ is declining as $z^{-5/3}$. Thus, there is a sharply declining visible radiation at the flame tip, while the total, mostly infrared, radiation from the plume declines more slowly.

Measurements of visible flame length $L_v$ and tilt angle $\theta$ reported for field tests provide a way to evaluate the validity of the model predictions, as embodied in the relations of Eqs. (30) and (38). We utilize the compilations of 33 tests from Moorhouse [18], Johnson [19], and Nedelka et al. [20]

[9] Since $c$ is to represent $\bar{w}_f$, which is proportional to $F_f^{1/5}$, the latter must also be a parameter in the general relation that (38) represents. Given the small range of $F_f^{1/5}$ in the experiments, it can be neglected.

[10] These are steady pool fires in thermally insulated containers with negligible heat transfer from the substrate to the liquid pool.

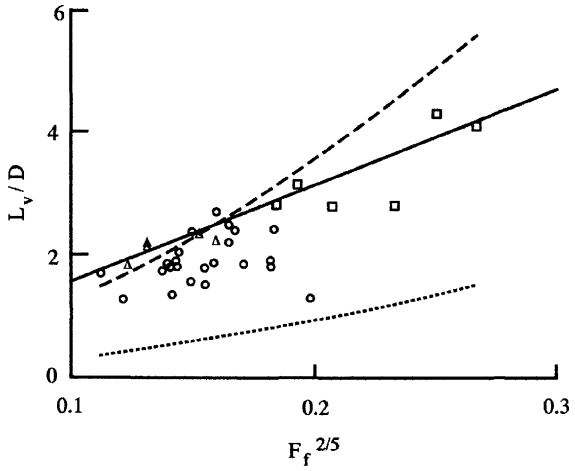


Fig. 5. A plot of the measured visible flame length $L_v$ of LNG pool fires compared to (43) [solid line]. Triangles are circular adiabatic pool fires; circles are rectangular adiabatic pool fires; squares are circular pool fires on water. The Thomas correlation of (44) is show as a dashed line, and the combustion zone height $L_c$ of (41) is shown as a dotted line.

for adiabatic LNG pool fires.[11] These cover a range of effective pool diameters[12] $D = 1.8$–$35$ m, wind speeds $V = 1.8$–$14.4$ m/s, flame lengths $L_v = 3.3$–$77$ m, and tilt angles $\theta = 28$–$66°$; more than an order of magnitude variation in all observables except tilt angle. In addition, we include six tests of unconfined non-adiabatic steady state circular LNG pool fires on water [21].

We first examine in Fig. 5 the scaling relation described by Eq. (30). We distinguish three types of pool fires: circular adiabatic (triangles), rectangular adiabatic (circles), and circular non-adiabatic pool fires on water (squares). In Section 4 below we argue that the rectangular pools are sensitive to wind direction, and should be treated separately from the circular pools in any correlation. Considering only the circular pools, a linear regression of (30) gives $z_0/D \simeq 0$, and the correlation becomes

$$\frac{L_v}{D} = 15.5(1 \pm 0.095) F_f^{2/5} \quad \text{(circular)} \tag{43}$$

and is shown as the solid line in Fig. 5. The rectangular pool fires are clearly distinguishable from the circular ones, showing considerably more scatter and smaller values of $L_v/D$.[13]

The correlation of Thomas [6] for wood crib fires, widely used for pool fires, is

$$\frac{L_T}{D} = 42(F_f)^{0.61} \tag{44}$$

This correlation is plotted in Fig. 5 as a dashed line, where it can be seen that it overestimates the visible flame length at large values of $F_f$. Also shown is the correlation (41) of the combustion zone length $L_c$ (dotted line), clearly only a minor fraction of the visible plume length.

[11] Of these, 7 were circular and the remaining were rectangular with aspect ratios between 1 and 2.5.

[12] The effective pool diameter for a non-circular shape equals four times the pool area divided by its perimeter.

[13] See Section 4.

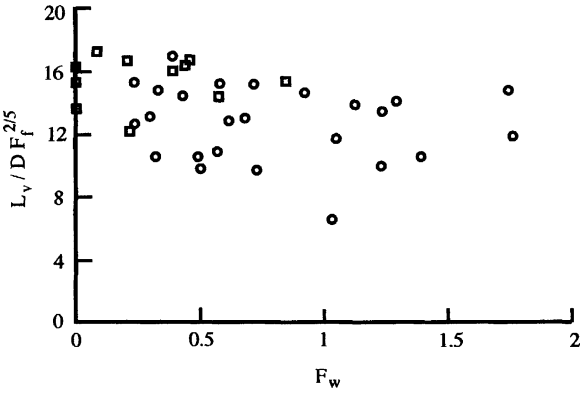


Fig. 6. A plot showing the dependence of visible flame length on wind speed for LNG pool fires. Squares are circular pool fires, both adiabatic and on water; circles are rectangular adiabatic pool fires.

To show how the visible flame length depends upon wind speed, we plot $(L_v/D)F_f^{-2/5}$ versus the wind Froude number $F_w \equiv V/\sqrt{gD}$ in Fig. 6 (squares for circular pools, circles for rectangular ones). For either group, there is no clear dependence upon wind Froude number, more certainly for the circular pools.

### 2.3.3. Wind tilt

As detailed in Section 2.1.5, the sine of the flame tilt angle $\theta$ should be a function of the wind Froude number $F_w$. Fig. 7 shows the measured values of $\sin\theta$ as a function of $F_w$. Also shown is the best correlation using the relation of (38),

$$\sin\theta = \frac{F_w}{F_w + 0.19} \tag{45}$$

for which $r = 0.62$. It is remarkable that the field tests predominantly show tilt angles greater than 30°, and that (45) indicates that $F_w$ would have to be less than 0.03 for $\theta$ to be less than 10°. Evidently pool fire tilt is very sensitive to wind speed at low speeds ($F_w \ll 0.2$) but insensitive at high speeds ($F_w \gg 0.2$).

An empirical relation for wind tilt has been given by Rew and Hurlbut [22]

$$\frac{\tan\theta}{\cos\theta} = 3.13 F_w^{0.431} \tag{46}$$

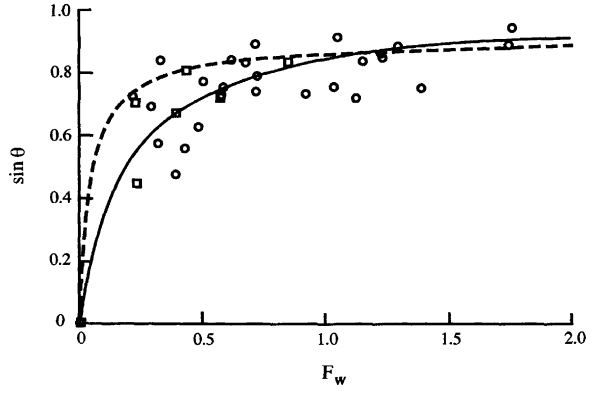


Fig. 7. A plot of the sine of the wind tilt angle $\theta$ as a function of the wind Froude number $F_w = V_w/\sqrt{gD}$. The solid line is the empirical correlation of Eq. (45); symbols as in Fig. 6. The dashed line is the wind tilt relation of Rew and Hurlbert [22].

This is shown in Fig. 7 as a dashed line. It overpredicts the wind tilt at low wind Froude number, most likely because of the unphysical limit that $d(\sin\theta)/dF_w = \infty$ at $F_w = 0$.

The comparisons of the pool fire model with the observations in field experiments, for flame length $L_v$ in Fig. 5 and flame tilt angle $\theta$ in Fig. 7, show considerable variability. The model input variables $\rho_a$, $\dot{m}$, $D$, and $V$ are fairly well determined. On the other hand, measurements of $L_v$ and $\theta$ are somewhat uncertain since the plume outline, on which they are based, is quite variable in time and difficult to specify accurately. For the larger pool diameters, copious soot formation may obscure the flame shape and especially the determination of its length.

Comparisons of model and observed trajectories of thermal plumes in a cross wind, which like pool fires are strongly influenced by buoyancy, show similar variability [15,16]. Fay, Escudier, and Hoult [16] report that the standard deviation of over 500 measurements in plume rise height is about 15% of the mean value, larger than the 10% deviation for the pool flame length of Eq. (43). Evidently such measurements exhibit an irreducible level of variability.

## 3. Thermal radiation model

Numerous measurements of thermal radiation from pool fires have been correlated with grey gas models of the fire zone or with surface emissive power models of the flame surface (see [4,22]). For small diameter pool fires, soot concentrations can be low enough that the flame zone is nearly transparent, and a grey gas model provides a satisfactory correlation. On the other hand, very large pool fires exhibit copious soot formation that can obscure thermal radiation, especially from the upper portion of the flame zone. For these fires a surface emissive power model provides better evidence for extrapolating the measurements to very large pool fires, of a size well beyond what has been observed in field experiments.

In this section we develop a grey gas model of thermal radiation from the combustion and plume zones of a pool fire that is consistent with the pool fire model portrayed in Fig. 1 and analyzed in Section 2. It is based upon the assumption that the pool fire thermal radiation is emitted (and absorbed) by soot particles in both zones, and that the soot emissivity within these zones is proportional to the local concentration of products of combustion, independent of the size of the pool fire. In effect, this is equivalent to assuming that a fixed fraction of the fuel carbon is converted to soot particles of fixed emissive properties. A consequence of this model is that the optical width of the pool fire will scale linearly with the height $z$. This scaling factor can be determined from field measurements of pool fire surface emissive power. According to this model only two empirical constants are needed to predict the thermal radiation from pool fires of any size, for a given fuel.

### 3.1. Grey gas pool fire model

In a pool fire, both the combustion zone, the region within which the air and fuel mix and react, and the plume zone, where further mixing with excess air occurs, emit thermal radiation to the surrounding atmosphere. At the flame surface in the combustion zone, where combustion reactions take place, the temperature reaches a peak value, $T_f$, as does the concentration of stoichiometric combustion products. In a diffusion flame, if the mass and thermal diffusivities are equal, any species mass fraction is linearly related to the temperature [11]. Assuming this is so for the pool fire, the mass fraction of products $\chi_p$ is given by (1) and the corresponding mass density of combustion products, $\rho\chi_p$, to which the soot emissivity, $\kappa$, is proportional, is

$$\kappa \propto \rho\chi_p = \frac{\rho T - \rho T_a}{T_f - T_a} = (\rho_a - \rho)\frac{T_a}{T_f - T_a} \tag{47}$$

Thus, the soot emissivity is proportional to $(\rho_a - \rho)$, a function that varies only gradually with radial distance at any level $z$ within the pool fire, until it rapidly approaches zero at the outer edge, where $\rho = \rho_a$. As a useful approximation, we may regard the soot density, and thereby the grey gas emissivity, $\kappa$, to be constant throughout the pool fire [23].

We now proceed to calculate the flame emissive power $\varepsilon$ at the outer surface of the pool fire zones. We consider a horizontal slice of the flame zone, of width $b$ as shown in Fig. 1. The radiating region, where $T^4$ is only substantial if $T$ is close to the peak temperature $T_f$, having a radial extent of $\gamma b$ which is small compared to $b$, provides an outward heat flux of $\sigma T_f^4 \kappa\gamma b$, where $\sigma$ is the Stefan-Boltzmann constant. This radial flux is attenuated by absorption, by a factor $\exp(-\kappa b)$, resulting in a surface emissive power $\varepsilon\{b\}$ of[14]

$$\varepsilon\{b\} = \sigma T_f^4[\kappa\gamma b \exp(-\kappa b)] \tag{48}$$

Recognizing that the lateral flame zone dimensions $b$ is proportional to $z$ [see Eqs. (6), (7), (22), and (28)], we may replace $\kappa b$ by $kz$ so that (48) takes the form

$$\frac{\varepsilon\{z\}}{\gamma\sigma T_f^4} = kz\exp(-kz) \tag{49}$$

where the scaled absorption coefficient $\kappa \equiv \kappa b/z$. The emissive power $\varepsilon$ has a maximum at $kz = 1$, at which $\varepsilon/\gamma\sigma T_f^4 = 1/e$.

Wide angle radiometric measurements of flame thermal radiation are interpreted as defining an average surface emissive power $\langle\varepsilon\rangle$, averaged over the exterior of the flame zone. For the radiation model of Eq. (49), this average becomes[15]

$$\frac{\langle\varepsilon\{L_v\}\rangle}{\gamma\sigma T_f^4} = \frac{1}{L_v}\int_0^L kz\exp(-kz)\,dz = \frac{1}{kL_v}[1 - (1 + kL_v)\exp(-kL_v)] \tag{50}$$

This average surface emissive power is plotted in Fig. 8 as a function of the flame optical length $kL_v$. For small flames ($kL_v \ll 1$), $\langle\varepsilon\{L_v\}\rangle/\gamma\sigma T_f^4 = kL_v$, while for very large flames

[14] In the combustion zone, this relation is exact for $\gamma \ll 1$, but only approximate in the plume zone, which has conical, rather than cylindrical, symmetry.

[15] Here we assume that $T_f^4$ does not vary much for $0 < z < L_v$.

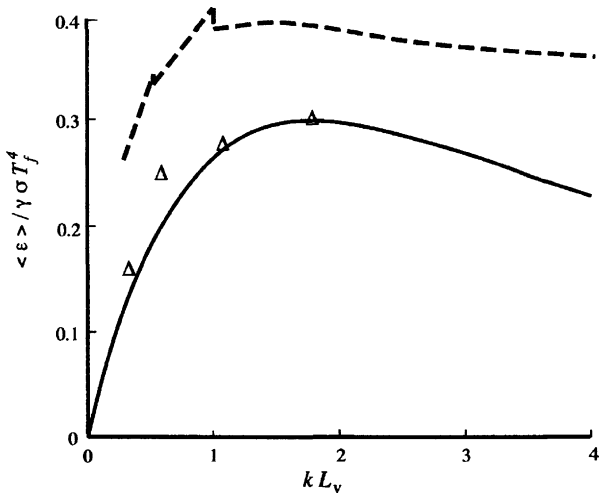


Fig. 8. The average surface emissive power $\langle\varepsilon\rangle$ as a function of the flame optical length $kL_v$ (solid line). Measured values for LNG pool fires are indicted by Δ. Dashed line is the model of Rew and Hulbert [25].

$\langle\varepsilon\{L_v\}\rangle/\gamma\sigma T_f^4 = 1/kL_v$. At $kL_v = 1.795$, $\langle\varepsilon\{L_v\}\rangle/\gamma\sigma T_f^4$ reaches a maximum value of 0.2984. For very large pool fires ($kL_v \gg 1$), thermal radiation is significant only in a strip of height $\sim k^{-1}$ at the base of the fire, and amounts to a thermal flux per unit perimeter of $\gamma\sigma T_f^4(k^{-1})$ and total thermal flux of $\gamma\sigma T_f^4(k^{-1}\pi D)$.

### 3.1.1. Comparison with LNG field tests

In this section we compare the grey gas model for the average surface emissive power with the measurement analysis reported by Nedelka et al. [20] for large scale tests of adiabatic LNG pool fires confined within circular dikes of diameters 6.1, 10.6, 20, and 35 m. In their analysis, the Thomas visible flame length (44) and wind tilt were used to define a cylindrical flame shape, although the actual flame shape was somewhat different. Nevertheless, this comparison should be valid for use in predicting thermal radiation for pool fires of other sizes, including larger ones.

In making this comparison, we have two parameters, $k$ and $\gamma\sigma T_f^4$, to select to match the implied value of $\langle\varepsilon\{L_v\}\rangle$ Assuming that the 35 m diameter test corresponds to the maximum $\langle\varepsilon\rangle$ of Fig. 8, we choose $k = 0.0233\ \mathrm{m}^{-1}$ and $\gamma\sigma T_f^4 = 563\ \mathrm{kW/m^2}$. The values of $\langle\varepsilon\rangle/\gamma\sigma T_f^4$ for the 6.1, 10.6, 20, and 35 m tests are shown in Fig. 8 as triangles. The fit is certainly satisfactory, and might be made slightly better by adjusting the parameter values.[16] In calculating the value of $\langle\varepsilon\rangle$ from the wide angle radiometer measurements, Nedelka et al. [20] assume that the local value of $\varepsilon\{z\}$ is everywhere equal to $\langle\varepsilon\rangle$. A more rigorous test of the model would require reevaluating the radiometer measurements using the model distribution (49) in arriving at the optimum values of the model parameters.

According to the model, the local value of $\varepsilon\{z\}$ reaches a maximum at $kz = 1$ ($z = 42.9$ m), at which $\varepsilon = 207\ \mathrm{kW/m^2}$. The latter is about 20% larger than the maximum of $\langle\varepsilon\rangle$. Narrow angle radiometer measurements of $\varepsilon$ for 20 m diameter and smaller tests have lower values than $207\ \mathrm{kW/m^2}$, but similar measurements for the 35 m diameter fire are 50% higher [20]. The discrepancy lies in the method for predicting the flame shape. The model parameter values are suitable for estimating total thermal radiation from a pool fire incident upon a distant receptor, and may not accurately predict local values of $\varepsilon$.

Finally, we note that the the limiting value of the emitted thermal flux per unit of pool circumference is $\gamma\sigma T_f^4 k^{-1} = 24.2\ \mathrm{MW/m}$.

A premise of the grey gas model is that the region of emitting gas near the flame surface is a small fraction $\gamma$ of the flame zone thickness. If the flame temperature $T_f$ is close to the adiabatic flame temperature of about 2300 K, then $\gamma = 0.36$. While not exactly small, this value is consistent with the assumption of a peaked temperature distribution within the flame zone.

The grey gas model described above for large pool fires is in some respects similar to that used by Fay et al. [25] to analyze measurements of thermal radiation from laboratory scale fireballs. As noted in Section 2.2, the unsteady burnup of a fireball mimics that of a large scale eddy in a pool fire. Fay et al. [25] note that the thermal radiation pulse of the fireball extends beyond the time of visible burnup, about 15% of the total radiation being emitted after visible radiation has ceased. It is likely that, for pool fires, a similar percentage of the wide-angle radiometric flux emanates from the hot gases above the visible flame tip. Nevertheless, the decline in imputed fireball temperature with time beyond the disappearance of visible radiation is precipitous, as it is with the modeled temperature in the pool fire plume zone (27). For the laboratory fireballs, where the initial fuel sample volume did not exceed $200\ \mathrm{cm^3}$, the grey gas absorption coefficient $k$ is about an order of magnitude larger than that quoted above for large LNG pool fires. Even so, the largest value of $kL_v$ for the fireball experiments was 0.07, quite small compared with the values shown in Fig. 8, where soot absorption is important in limiting surface emission.[17]

Rew and Hulbert [22] have proposed a generic model (POLFIRE6) for thermal radiation from pool fires of various fuels, with fuel-specific parameters derived from experimental observations. This model incorporates the effects of soot absorption as a function of pool diameter and fuel type. For LNG fuel, the POOLFIRE6 results are shown in Fig. 8 as a dashed line. Over the range of measurements shown, the POOLFIRE6 model results are higher than the measurements by about 50%. For very large values of $kD$, there is an even greater discrepancy between the POOLFIRE6 model and the grey gas model of this paper. Rew and Hulbert [22] note that, at distances large compared with $D$, their model predicts receptor heat fluxes about 1.5 times the measured values. For the closest distances, about $2D$, the mean overprediction is about 200%.

[16] Nedelka et al. [20] emphasize that a reported $\langle\varepsilon\rangle$ is associated with a corresponding given flame shape and area. We have used the value for a cylinder of diameter $D$ and length $L_v$.

[17] Tien et al. [24] list a value of $k$ for methane flames that is 100 times that for the LNG pool fires. It is likely that the extremely large Reynolds number of the field experiments has an important effect on the value of $k$.

*3.1.2. Thermal flux to a receptor*

The thermal flux $q$ to a receptor at a distance $x$ from the edge of a pool fire can be calculated using the appropriate view factor $F$, such as that given by Sparrow and Cess [26] for a cylindrical untilted fire. In the case of large pool fires ($kL$, $kD \gg 1$), where the thermal radiation is emitted from a region at the base of the fire, of height $k^{-1}$, and thereby tilt can be ignored, the view factor is somewhat simplified for distances $kx \gg 1$. The source emission may be considered to have a uniform value of $\gamma\sigma T_f^4$ over the height $k^{-1}$, leading to[18]

$$\frac{q}{\gamma\sigma T_f^4} = F\{X, Y\} \tag{51}$$

where

$$F = \frac{X}{\pi Y}\left(\frac{2}{\sqrt{Y^2-1}} + \frac{Y^2+1}{Y^2-1} arctan\sqrt{\frac{Y+1}{Y-1}} - arctan\sqrt{\frac{Y-1}{Y+1}}\right)$$

$$X \equiv \frac{1}{kR}; \quad Y \equiv 1 + \frac{x}{R}; \quad R \equiv \frac{D}{2} \tag{52}$$

and provided $kx \gg 1$ and $kR \gg 1$. In the limits of $x/R \gg 1$ and $x/R \ll 1$, respectively, (52) reduces to

$$\frac{q}{\gamma\sigma T_f^4} = \frac{2R}{\pi k x^2}; \quad \frac{x}{R} \gg 1 \text{ or } = \frac{1}{2kx}; \quad \frac{x}{R} \ll 1 \tag{53}$$

For a practical calculation, atmospheric absorption over the distance $x$ must be taken into account.

## 4. Mass evaporation rate of pool fires

### 4.1. Adiabatic pool fires

In the previous sections we have treated the fuel mass evaporation rate $\dot{m}$ as an exogenous variable, one that is measured in a laboratory or field experiment. It is an essential component of the fuel Froude number (Eq. (3)), the dimensionless scaling variable of the pool fire model. But it is generally recognized that the fuel evaporation rate for adiabatic pool fires is determined by heat transfer from the pool fire, a self sustaining feedback mechanism that should be determinable from the pool fire model itself.

For pool fires that are clearly turbulent, which is true for pool diameters $D$ more than 1 m, the observed mass evaporation rate for a variety of fuels can be approximated by a function of the fuel heating value $h_c$ and heat of vaporization $h_v$ (see [4]),

$$\dot{m} = (1 \times 10^{-3}\,\mathrm{kg/m^2\,s})\frac{h_c}{h_v} \tag{54}$$

For common hydrocarbon fuels, $h_c \simeq 45$ MJ/kg fuel, so that the implied evaporative heat transfer rate to these fuels, $\dot{m}h_v$, is 45 kW/m$^2$.

[18] The first term in the parenthetical expression for $F$ in (52) is higher by a factor of two than the corresponding value given in [26], which is in error.

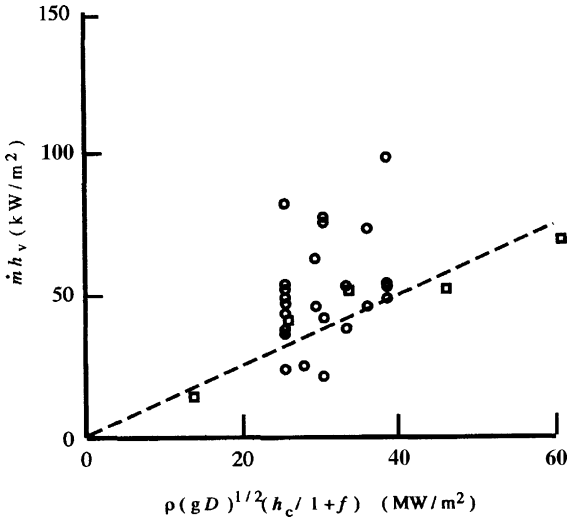


Fig. 9. The fuel evaporative heat flux $\dot{m}h_v$ as a function of the convective enthalpy flux $\rho\sqrt{gD}h_c/(1+f)$ for adiabatic LNG pool fires. The dashed line is Eq. (56). Circles are rectangular pools; squares are circular pools.

Hottel (see [4]) argued that the heat flux $\dot{m}h_v$ to the liquid fuel is a combination of radiative and convective heat transfer from the flame gas, and while convective heat transfer dominates for small diameter laminar fires, radiant transfer is controlling for large, turbulent fires. Whether or not this is true, we suggest that the evaporative heat transfer may be written as the sum of these components, modeled as

$$\dot{m}h_v = a\left(\rho_a\sqrt{gD}\left[\frac{h_c}{1+f}\right]\right) + b\langle\varepsilon\rangle \tag{55}$$

where the dimensionless coefficient $a$ is the Stanton number for the convective flow and the coefficient $b$ would contain view factors for the radiant heat transfer from the flame zone to the fuel surface. Both the convective and radiative terms in (55) are dependent on the pool diameter $D$, in contrast to the empirical relation (54).

If we assume that the radiant heat transfer is small compared to convection, we can compare the measured heat transfer rate $\dot{m}hv$ for LNG pool fires with the proposed relation of (55), as shown in Fig. 9. We note that the circular pool fires have lower evaporation rates than rectangular pools, and less variation about the mean value. We ascribe this difference to two causes, the presence of right angle corners in the rectangular pools and the asymmetry with respect to the wind direction, which could affect the flow in the recirculation zone and the consequent heat transfer rate to the pool surface. Treating the circular and rectangular pool measurements separately, the correlations of the convective heat transfer rates become

$$\dot{m}h_v = 1.30 \times 10^{-3}(1 \pm 0.19)\left(\rho_a\sqrt{gD}\left[\frac{h_c}{1+f}\right]\right) \text{ (circular)} \tag{56}$$

$$= 1.75 \times 10^{-3}(1 \pm 0.34)\left(\rho_a\sqrt{gD}\left[\frac{h_c}{1+f}\right]\right) \text{ (rectangular)} \tag{57}$$

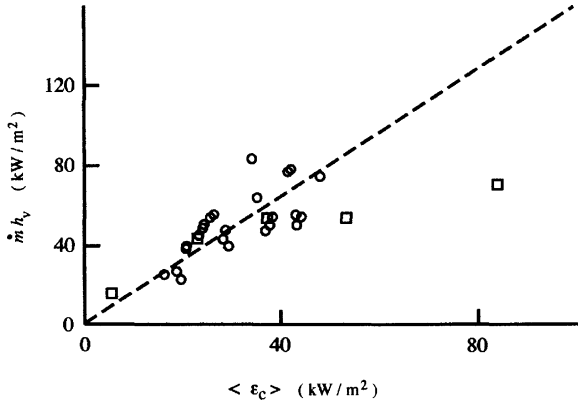


Fig. 10. The fuel evaporative heat flux $\dot{m}h_v$ as a function of the combustion zone surface emissive power $\langle\varepsilon_c\rangle$ for LNG pool fires. The dashed line is Eq. (58). Circles are rectangular pools; squares are circular pools.

where (56) is plotted in Fig. 9 as a dashed line. There is a trend of enhanced evaporation rate with increasing pool diameter. In addition, Eqs. (56) and (57) have the form of (54) insofar as the fuel heat properties are concerned. Also, the Stanton number is the same order of magnitude as that for turbulent heat transfer from a flat plate.

On the other hand, if we assume radiation dominates, we find[19]

$$\dot{m}h_v = 1.6(1 \pm 0.23)\langle\varepsilon_c\rangle \tag{58}$$

where $\langle\varepsilon_c\rangle$ is the average surface emissive power in the combustion zone, the portion of the pool fire that is closest to the pool surface, as shown by the dashed line in Fig. 10 for adiabatic LNG pool fires. There is no distinction between the circular and rectangular pool shapes, both showing about the same mean values and deviation.Within the range of $D$ for these tests, $\langle\varepsilon_c\rangle$ increases gradually with $D$, as in (56).

On the basis of this comparison with the LNG tests, either convection or radiation, or a combination of both, could account for the measured fuel evaporation rate. But there are other reasons to prefer convection as the dominant heat transfer mechanism, contrary to Hottel's suggestion. Hydrogen pool fires,which are correlated by Eq. (54), and presumably (56), would experience a much smaller radiant flux since they are not luminous, and therefore would not be explained by (58). In addition, for large enough diameters, $\langle\varepsilon\rangle$ (and radiant heating) decreases as $D^{-1}$, so that convective heating must dominate at very large diameters. For these reasons, we suggest (56) is a more reliable model for correlating fuel evaporative rates of pool fires.

If one accepts this argument, and that the effect of fuel properties on $\dot{m}$ are expressed as in (56) and (57), the expected fuel Froude number $F_f^*$ for circular and rectangular pool fires, derived from (56) and (57), are found to be

$$F_f^* = 1.30 \times 10^{-3}\left(\frac{h_c}{(1+f)h_v}\right) = [7.01 \times 10^{-3}]_{LNG} \quad \text{(circular)} \tag{59}$$

$$F_f^* = 1.75 \times 10^{-3}\left(\frac{h_c}{(1+f)h_v}\right) = [9.45 \times 10^{-3}]_{LNG} \quad \text{(rectangular)} \tag{60}$$

where the second expression on the right of (59) and (60) is the value for LNG.

The general relationship between $L_v$ and $F_f$, expressed in (43), must hold for these adiabatic pool fires. This relationship becomes

$$\left(\frac{L_v}{D}\right)^* = 1.12\left(\frac{h_c}{(1+f)h_v}\right)^{2/5} = [2.19]_{LNG} \quad \text{(circular)} \tag{61}$$

$$\left(\frac{L_v}{D}\right)^* = 0.97\left(\frac{h_c}{(1+f)h_v}\right)^{2/5} = [1.90]_{LNG} \quad \text{(rectangular)} \tag{62}$$

It is notable that the rectangular pool fire experiences a greater vapor generation rate ($F_f^*$) but lesser visible flame height, compared with the circular pool. This reflects a greater mixing within the combustion zone, and hence increased heat transfer to the fuel, as well as in the plume zone, thereby shortening the flame length, incurred by the irregular rectangular pool shape compared with the circular one. These are not large differences, but are easily detectable in the experiments (see Figs. 5, 6, and 9).

The relations (59)–(61), based upon the convective heat transfer model of (56) and (57), show that there are universal values of $F_f^*$ and $L_v^*/D$ for all adiabatic pool fires that are only modestly dependent upon dimensionless pool shape and and fuel thermal property parameters. While individual experimental values show deviation from this average, none of this scatter can be reduced by taking into account wind speed or flame tilt.

### 4.2. Non-adiabatic pool fires

Unconstrained pool fires formed above cryogenic fuels discharged onto water or land burn at greater rates $\dot{m}$ than do adiabatic pools of the same diameter. Heat transfer from the substrate adds to that from the combustion zone, increasing the evaporation rate by an amount $\Delta\dot{m}$ above that of the corresponding adiabatic pool fire. In estimating the size of LNG pool fires formed by the accidental discharge of cargo from marine tankers, for example, it is usual to assume that the evaporation rate $\dot{m}$ is constant irrespective of the conditions of the discharge (see [1,27]).

There is little experimental evidence justifying this assumption. Here we will use six tests of unconfined non-adiabatic steady state circular LNG pool fires on water [21] to examine the rate of evaporation augmentation, $\Delta\dot{m}$, and its dependence upon the test conditions.

In these tests, LNG was discharged at a steady mass flow rate $\dot{M}$ onto the surface of water for a sufficient length of time to establish a steady pool fire of constant unconstrained diameter $D$. In general, $D$ increased with increasing $\dot{M}$. The incremental mass evaporation rate $\Delta\dot{m}$ is calculated by subtracting the adiabatic

[19] We calculate $\langle\varepsilon_c\rangle$ using (50) evaluated for $L_c$, as given in (41).

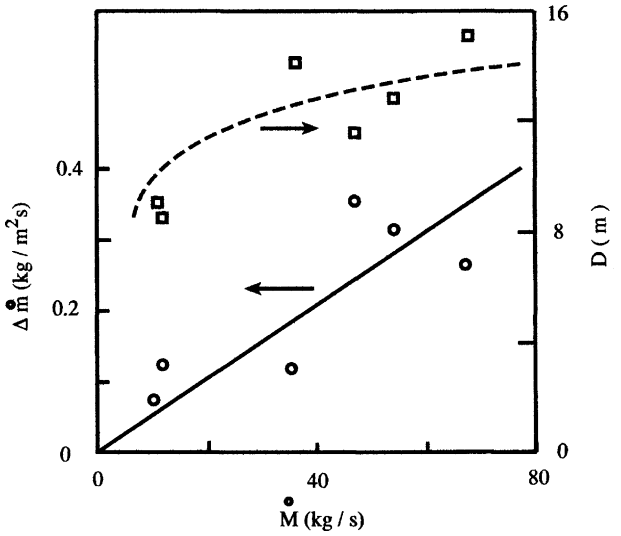


Fig. 11. The incremental mass evaporation rate, $\Delta\dot{m}$ (on left scale), and pool fire diameter, $D$ (on right scale), for unconstrained, non-adiabatic, steady pool fires on water, as a function of the steady mass flow rate $\dot{M}$ of supply (and combustion). The solid and dashed lines are the correlations of (65) and (63).

value of (56) from the gross evaporation rate

$$\Delta\dot{m} \equiv \frac{\dot{M}}{\pi D^2/4} - 1.30\times10^{-3}\left(\rho_a\sqrt{gD}\left[\frac{h_c}{(1+f)h_v}\right]\right) \quad (63)$$

The incremental mass evaporation rate $\Delta\dot{m}$ as a function of the mass flow rate $\dot{M}$ for these tests is plotted in Fig. 11, where it can be seen to be approximately linearly proportional to $\dot{M}$; $\dot{m}$ also increases with $\dot{M}$, as does the pool diameter. The rate of fluid flow into the pool has an important effect upon the burning rate and pool size.

To explain this effect, we propose that heat the transfer rate from the water to the pool fire is determined by the relative convective motion of the liquid fuel across the water surface in a manner similar to that of the combustion zone gases. Defining a Stanton number $St$ for this heat transfer by

$$St \equiv \frac{\Delta\dot{m}h_v}{\rho_1 V_1 C_p(T_a - T_1)} \quad (64)$$

where the subscript 1 identifies the pool liquid properties, $C_p$ is the water specific heat, and $V_1$ is the fuel radial convective velocity.[20] The measurements of Fig. 11 are correlated by

$$\Delta\dot{m} = 1.10\times10^{-4}\left(\frac{\rho_1 V_1 C_p(T_a - T_1)}{h_v}\right) \quad (65)$$

as shown by the solid line in Fig. 11. The Stanton number of $1.10\times10^{-4}$ is an order of magnitude smaller than that for combustion gas heating of (56). The corresponding correlation for diameter $D$, obtained from (63) and (65), is shown as a dashed line.

In applying these evaporation rates to unhindered spreading of spills on water, as in [1], where $D$ is determined as a function of time by the dynamics of gravitational spreading, the total mass evaporation rate $\dot{m}\{t\}$ becomes

$$\dot{m}\{t\} = 1.30\times10^{-3}\left(\rho_a\sqrt{gD}\left[\frac{h_c}{(1+f)h_v}\right]\right) + 1.10\times10^{-4}\left(\frac{\rho_1 V_1 C_p(T_a - T_1)}{h_v}\right) \quad (66)$$

where $V_1\{t\} = \mathrm{d}D\{t\}/2\mathrm{d}t$.

## 5. Conclusions

The fluid mechanical model of a pool fire described in Section 2, consisting of a combustion zone next to the base of the fire and a plume zone above it, provides a consistent scheme for developing non-dimensional scaling parameters for correlating and extrapolating significant pool fire physical properties over large ranges of the controlling physico-chemical constraints of pool fire occurrence. This model includes an integral formulation of the fluxes of mass, momentum, and energy in the pool fire, from which important observables such as combustion zone and visible flame lengths, flame tilt, flame emissive power, and fuel evaporation rate. The model incorporates non-dimensional parameters, some of which can be evaluated by comparison with field test observations. Knowledge of these parameters, together with the model analytical formulation, permits extrapolation of fire properties to larger size pool fires than have yet been tested.

This model is tested against field measurements of large scale pool fires, principally of LNG, having physical properties spanning more than an order of magnitude. The dimensionless combustion zone height and visible flame length depend only upon the fuel Froude number while the tilt angle depends only on the wind Froude number. Compared with circular pool fires, rectangular ones have somewhat different values for these dimensionless properties. While the agreement between the model and the field observations is not precise, only a few dimensionless constants are needed to correlate the observations. Periodic flow phenomena observed in pool fires are consonant with this fluid mechanical model.

A grey gas thermal radiation model, Section 3, builds on the entrainment model. It incorporates an assumption regarding the soot concentration that reflects the distribution of combustion products within the flame zone and which leads to a constant value of the soot emissivity throughout the flame region. A virtue of this model is that it produces a surface emissive power that varies continuously with height within the flame, achieving a maximum value within the visible flame length for sufficiently large fires. Comparison with average surface emissive power measurements from LNG pool fires shows good agreement with the model, and some confidence that it can be extrapolated reliably to larger scale fires.

A model of convective heat transfer from the combustion zone to the liquid fuel pool accounts for the variation of measured fuel evaporation rates in adiabatic pool fires. A consequence is that the dimensionless visible flame height and fuel Froude number are independent of pool diameter, depending only on fuel thermochemical properties. For non-adiabatic cryogenic pools

[20] For these tests, $V_1$ equals the ejection velocity from the pipe supplying the LNG to the fuel pool.

on water, a model of convective heat transfer from the substrate accounts for an incremental evaporation rate that depends upon outward flow of the fuel.

## References

[1] J.A. Fay, J. Haz. Mat. B96 (2003) 171–183.
[2] G. Heskestad, SPFE Handbook of Fire Protection Engineering, third ed., National Fire Protection Association, Quincy, 2002, 2-1 to 2-17.
[3] D.T. Gottuck, D.A. White, SPFE Handbook of Fire Protection Engineering, third ed., National Fire Protection Association, Quincy, 2002, 2-297 to 2-316.
[4] K.S. Mudan, Prog. Energy Combust. Sci. 10 (1984) 59–80.
[5] G. Heskestad, Phil. Trans. R. Soc. Lond. A356 (1998) 2815–2833.
[6] P.H. Thomas, Ninth Symposium (International) on Combustion, Academic Press, New York, 1963, pp. 844–859.
[7] B.L. Morton, G.I. Taylor, J.S. Turner, Proc. Roy. Soc. (Lond.) A234 (1956) 1–23.
[8] G. Heskestad, Fire J. 7 (1984) 25.
[9] J.A. Fay, D.H. Lewis Jr., Sixteenth Symposium (International) on Combustion, The Combustion Institute, Pittsburgh, 1976, pp. 1397–1405.
[10] F.R. Steward, Comb. Sci. Tech. 2 (1970) 203–212.
[11] J.A. Fay, J. Aero. Sci. 21 (1954) 681–689.
[12] S.P. Burke, T.E.W. Schumann, Ind. Eng. Chem. 20 (1928) 998–1004.
[13] F.P. Ricou, D.B. Spaulding, J. Fluid Mech. 11 (1961) 21–32.
[14] D.P. Hoult, J.A. Fay, L.J. Forney, APCA J. 19 (1969) 585–590.
[15] J.A. Fay, M.P. Escudier, D.P. Hoult, Atm. Env. 3 (1969) 311–315.
[16] J.A. Fay, M.P. Escudier, D.P. Hoult, APCA J. 20 (1970) 391–397.
[17] H. Koseki, T. Yumoto, Fire Technol. 24 (1988) 33–47.
[18] J. Moorhouse, The Assessment of Major Hazards, Institution of Chemical Engineers Symposium Series No. 71, Institution of Chemical Engineers, Rugby, 1982, pp. 165–180.
[19] A.D. Johnson, Major Hazards Onshore and Offshore, Institution of Chemical Engineers Symposium Series No. 130, Institution of Chemical Engineers, Rugby, 1992, pp. 507–557.
[20] D. Nedelka, J. Moorhouse, R.F. Tucker, Proceedings of the Ninth International Congress and Exposition of Liquefied Natural Gas, vol. 2, no. III-3, Institute of Gas Technology (Chicago, 1990), 1990, pp. 1–23.
[21] P.P.K. Raj, A.N. Moussa, K. Aravamudan, Experiments involving pool and vapor fires from spills of liquefied natural gas on water, CG-D-55-79, ADA 077 073, U.S. Coast Guard, Washington DC, 1979.
[22] P.J. Rew, W.G. Hulbert, Development of pool fire thermal model, HSE Contract Research Report No. 96/1996, W. S. Atkins Safety and Reliability, Epsom, 1996, ISBN 0 7176 1084 5.
[23] H.C. Hottel, A.F. Sarofim, Radiative Transfer, McGraw-Hill, New York, 1967.
[24] C.L. Tien, K.Y. Lee, A.J. Stretton, SPFE Handbook of Fire Protection Engineering, thrid ed., National Fire Protection Association, Quincy, 2002, 1-73 to 1-89.
[25] J.A. Fay, G.J. Desgroseilliers, D.H. Lewis, Comb. Sci. Tech. 20 (1979) 141–151.
[26] E.M. Sparrow, R.D. Cess, Radiation Heat Transfer, Brooks/Cole Pub. Co., Belmont, 1966.
[27] P.K. Raj, Comb. Sci. Technol. 19 (1979) 251–254.